PHYSICAL REVIEW B **109**, 184110 (2024)

Direct observation of a systematic spatial distribution pattern of structural vacancies in an In_2Te_3 crystal

Kaichi Saito,[1,*] Yuichiro Hayasaka,[2] and Kenji Hiraga[3]
[1]*Department of Materials Science, Akita University, Akita 010-8502, Japan*
[2]*The Electron Microscopy Center, Tohoku University, Sendai 980-8577, Japan*
[3]*Institute for Materials Research, Tohoku University, Sendai 980-8577, Japan*

(Received 22 September 2023; revised 22 March 2024; accepted 6 May 2024; published 17 May 2024)

Identifying the nature of domain structures within crystals is crucial for researching $A_2^{\mathrm{III}}B_3^{\mathrm{VI}}$ compounds aimed at microelectronics applications. This paper provides a credible and convincing set of microscopic data on the domain structure formed in the high-temperature phase of an In_2Te_3 crystal (zinc-blende type structure), resolving a long-standing debate regarding the domain boundaries and structural vacancies in this crystal family. The crystal exhibited a finely subdivided matrix comprising parallelogram-shaped domains, each bounded by {111} planes. The domain boundaries were identified as a type of 180° domain wall, across which the crystal structure underwent a unit-cell inversion between parallel and antiparallel states. The domain interiors comprised a series of regionally varied structural units according to a statistically random, but a systematic spatial distribution pattern of structural vacancies induced along the [001] type direction. Consequently, the local structure gradually reversed between the two opposite corners defined along the longitudinal axis of each domain.

DOI: 10.1103/PhysRevB.109.184110

I. INTRODUCTION

Compound semiconductors comprising chemical elements belonging to groups III and VI of the periodic table, denoted as $A_2^{\mathrm{III}}B_3^{\mathrm{VI}}$ (A = Al, Ga, or In and B = S, Se, or Te), exhibit potential applications in future microelectronic devices [1–8]. These compounds pose significant challenges because of their physical and structural properties derived from the mismatch in valence between groups III and VI elements. Moreover, they exhibit highly defective structures and diverse crystal polymorphism depending on growth conditions. In previous studies, for instance [9], these compounds have been shown to exhibit a wurtzite or zinc-blende structure based on tetrahedral covalent bonding between the group III and VI atoms. In these structures, some equivalent lattice sites were only partially occupied, whereas other sites were vacant. Specific vacancies are known as *structural vacancies*, which are essential for stabilizing these compounds [10,11] and are different from atomic vacancies statistically distributed in crystals.

Among the members of the above-mentioned family, In_2Te_3 has been the subject of confusion and controversy considering its structural characteristics in the existing literature [12–29]. The phase diagram for the In-Te system has been examined and revised several times since it was first reported in the 1930s [22]. Currently, the diagrams reviewed and refined by Shunk [23], Zlomanov [24], and White and Okamoto [25] are a few of the most widely accepted versions. Previously reported x-ray diffraction (XRD) studies revealed that In_2Te_3 crystallizes in two polymorphic states depending on temperature. At high temperatures, it adopts a β phase with a zinc-blende type structure and fully disordered vacancies ($a = 0.6158$ nm; space group $F\bar{4}3m$) [12,13], whereas at low temperatures, it adopts an α phase with an antifluorite structure and regularly ordered vacancies ($a = 1.84$ nm; space group $F\bar{4}3m$) [14,16,17]. The former transforms into the latter at ~620 °C. The phase transformation of the In_2Te_3 crystal was once considered a type of order-disorder transformation [15], but was later suggested to be an order-mesoscopic transformation [26,27]. Researchers have elucidated the structural features of similar compounds such as Ga_2Te_3 [28–31], Ga_2Se_3 [9,31,32], and In_2Te_3 [26–29]. Moreover, the spatial distribution patterns of structural vacancies existing in these crystals were examined by high-resolution transmission electron microscopy (HRTEM) and selected-area electron diffraction (SAD) analyses. Prior studies supported the assumption that the low-temperature phases of these compounds exhibited orderly arranged vacancies in the crystalline matrices, and the high-temperature phases segregated the structural vacancies into subsets of {111}-lattice planes, forming domain structures. Particularly for high-temperature phases, the structural models developed based on the microscopic data mentioned above, describing a mesoscopic superstructure with multiple lattice intervals of two-dimensional {111} vacancy planes, were considered a stereotype of the domain structures commonly observed in $A_2^{\mathrm{III}}B_3^{\mathrm{VI}}$ compounds [9,26–32]. However, data obtained from the HRTEM images and the corresponding SAD patterns alone are insufficient to support the theory because these conventional techniques cannot be used to identify the constituent atoms or vacancies. Therefore, identifying the boundaries as vacancy-enriched planes is only a rough conclusion. Currently, the domain structures and

---

[*] Corresponding author: ksaito@gipc.akita-u.ac.jp

spatial distribution state of structural vacancies in the $A_2^{\mathrm{III}}B_3^{\mathrm{VI}}$ compounds remain largely unclear.

Spherical aberration corrector devices have recently revolutionized the performance of transmission electron microscopy (TEM) and scanning transmission electron microscopy (STEM) instruments. STEM combined with a spherical aberration corrector (probe-corrected STEM) has enabled unprecedented real-space imaging and spectroscopy for many materials at spatial and energy resolutions typically reaching the subangstrom and sub-electronvolt scales, respectively. The probe-corrected STEM has significantly improved the imaging of real domain structures formed in ferroelectric perovskite oxides [33–37]. The combination of probe-corrected STEM and energy-dispersive x-ray spectroscopy (EDXS) will facilitate the exploration of the domain structures formed in the $A_2^{\mathrm{III}}B_3^{\mathrm{VI}}$ compounds.

This study was focused on the high-temperature β-In_2Te_3 phase and provided a credible and convincing set of microscopic data based on probe-corrected STEM/EDXS for characterizing the real domain structure of the β-In_2Te_3 phase. The possibility of imaging the systematic spatial distribution pattern of structural vacancies induced for crystal stabilization is also discussed.

II. MATERIALS AND METHODS

An In_2Te_3 bulk ingot was prepared using a mixture of high-purity (5N each) In and Te. The components were alloyed in stoichiometric proportions in an evacuated ($\sim 10^{-3}$Pa) quartz capsule heated at 1000 °C for 24 h, followed by quenching in water. Subsequently, the quenched crystal was isothermally aged at 650 °C for 72 h to obtain the high-temperature β phase with a zinc-blende structure [12,13].

Powder XRD of the aged alloy was performed on a conventional θ-2θ diffractometer (RINT 2000, Rigaku) using Cu $K\alpha$ radiation ($\lambda = 0.154$ nm) under an air atmosphere at room temperature. Flakes of the alloy sample, prepared by crushing the aged ingot, were used as TEM/STEM samples. A transmission electron microscope (JEM-2100F, JEOL) was used to obtain HRTEM images and SAD patterns. A Titan3 G2 60-300 probe corrector (Thermo Fisher Scientific) combined with a Super-X EDXS system, which provides a minimum probe size of approximately 0.07 nm with a convergence semiangle α of ∼18 mrad, was additionally used to image high-angle annular dark-field STEM (HAADF-STEM) and EDXS data. For HAADF-STEM imaging, the annular detector was set to collect electrons scattered at angles between 79 and 120 mrad. Image simulations were performed using WINHREM [38] and VESTA [39] software to evaluate the atomic-resolution STEM images and visualize the deduced crystal structure model. The specimen thickness used for the HAADF-STEM image simulations was suppositionally set to 15 nm.

III. RESULTS

The data obtained from the XRD, HRTEM, and SAD experiments performed on the specimens used in this study closely resembled those reported previously for the high-temperature β-In_2Te_3 phase [26,27,29]. Figure 1 shows the XRD pattern of the prepared polycrystalline specimen. All high-intensity peaks could be indexed to the zinc-blende type structure (lattice parameter $a = 0.6153$ nm; space group $F\bar{4}3m$). Figure 2 shows the [110] HRTEM micrographs recorded at two different magnifications, illustrating typical microstructural features of the formed domains, together

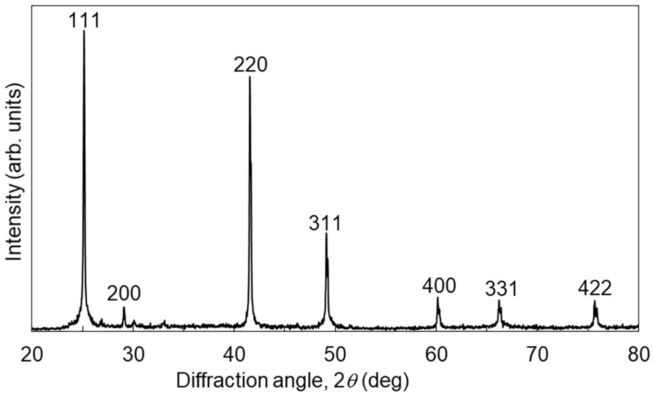

FIG. 1. Powder XRD pattern of high-temperature β-In_2Te_3 phase. All the peaks can be indexed to the zinc-blende type structure.

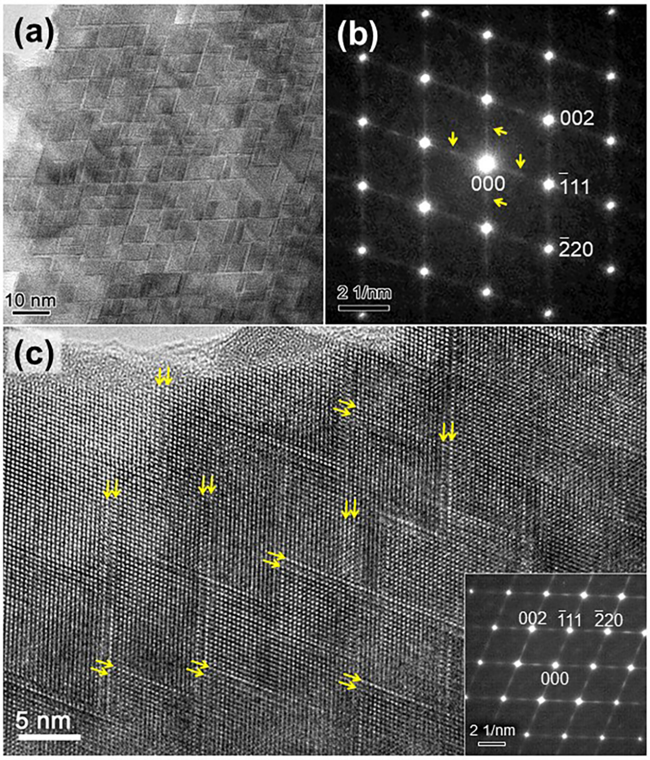

FIG. 2. (a) HRTEM image of the high-temperature β-In_2Te_3 phase along the [110] direction of the zinc-blende structure and (b) corresponding selected-area electron diffraction (SAD) pattern. (c) Enlarged [110] HRTEM image of a limited area shown in (a); the corresponding SAD pattern is shown in the inset. In (a), the intricate geometric contrast of parallelogram-shaped regions dividing the matrix is typical of the domain structure characteristic of this crystal. The SAD pattern reveals weak linear streaks along the ⟨111⟩ directions between fundamental spots, with their diffuse intensities maximized in the middle, as marked by arrows.

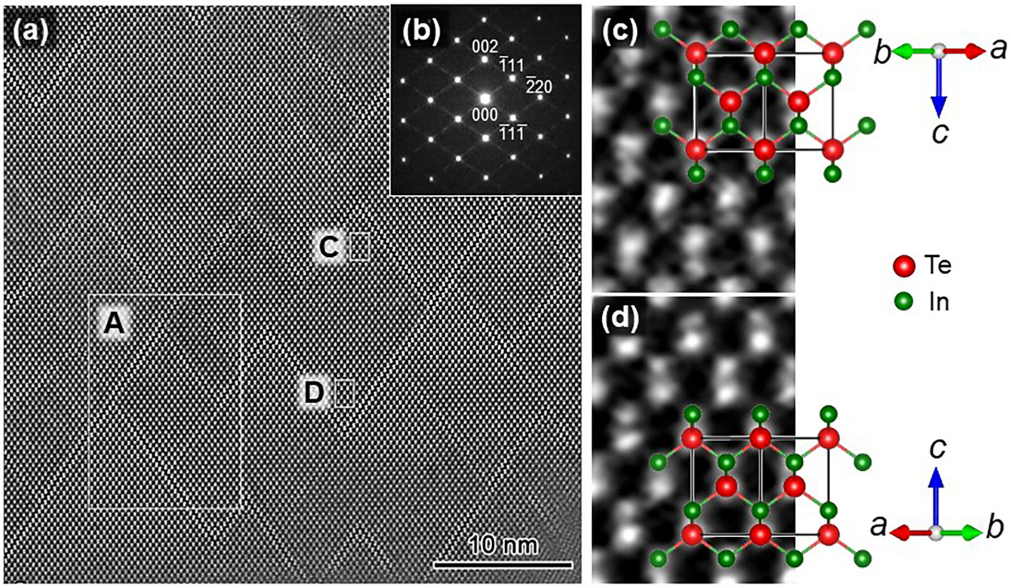

FIG. 3. (a) [110] HAADF-STEM image of the domain structure formed in the β-In_2Te_3 phase; the corresponding SAD pattern is shown in the inset (b). Individual domains present throughout the entire matrix have their crystallographic c axes pointing in the same direction, parallel to the [001] type direction. The individual domain located roughly in the middle of image (a), which contains the local regions marked by either C or D, has its crystallographic unit cell regionally inverted between the parallel and antiparallel states within the domain, as illustrated in (c) or (d) enlarged from the areas C or D, respectively, depicted in (a).

with the corresponding SAD patterns. Figure 2(a) presents an HRTEM image at an intermediate enlargement with poor visibility of minute details related to lattice contrast in the specimen. The corresponding SAD pattern is shown in Fig. 2(b). HRTEM imaging enables atomic-scale visualization of the domain structures formed in various crystalline materials. Figure 2(a) reveals a prominent contrast feature: the β-In_2Te_3 phase exhibits a crystalline matrix composed of various separate parallelogram-shaped regions (domains) of irregular shapes and sizes. This feature could be alternatively described as zigzags of the projection traces of plane defects parallel to the {111}-type planes [30]. The corresponding SAD pattern shows linear streaks connecting the fundamental Bragg reflection spots along the ⟨111⟩ type directions, with diffuse intensities maximized between the fundamental spots, as marked by the arrows [Fig. 2(b)]. These observations agree with the previously reported electron micrographic data on In_2Te_3 crystals prepared in a similar manner and some other $A_2^{\mathrm{III}}B_3^{\mathrm{VI}}$ compounds [9,26–32]. The linear streaks observed in the SAD pattern indicated some disorder in stacking along the ⟨111⟩ direction of the long-range ordered planes. The diffuse maxima between the fundamental spots indicate the presence of an undeveloped superlattice, characterized by the doubling of the period along the ⟨111⟩ type direction of the unit cell. Figure 2(c) depicts the [110]-HRTEM image of the domain structure recorded at a higher magnification together with the corresponding SAD pattern in the inset. This image shows a small-scale contrast feature comprising bright dots arranged in a rhombic cell, corresponding to the projected fundamental zinc-blende units of the β-In_2Te_3 crystal structure. Parallelogram-shaped domains at the atomic level are also evident, many of which are separated by pairs of double-spaced {111} type lattice planes with relatively high intensities, as marked by the paired arrows. The unique contrast feature recognized at the domain boundaries is attributed to certain lattice distortions or ionic displacements, as will be discussed later. However, the HRTEM image does not provide sufficient information for identifying the constituent atoms or structural vacancies. The diffuse maxima observed in the SAD pattern originate from the irregular distribution of the double-spaced {111} lattice planes, as indicated by the paired arrows. Moreover, such characteristic contrast features, which are observed in conventional HRTEM images of $A_2^{\mathrm{III}}B_3^{\mathrm{VI}}$ compounds, are attributed to the subsets of In{111} sublayers enriched with structural vacancies [9,26–32].

Atomic-scale HAADF-STEM was conducted on the current specimen using probe-corrected STEM to gain new insights into the domain structure observed through conventional HRTEM imaging. Figure 3(a) presents a typical atomic-scale HAADF-STEM image recorded from a microscopic region containing several domains, captured in the [110] incidence of the zinc-blende matrix. The corresponding SAD pattern is shown in Fig. 3(b). Figure 3(a) reveals numerous parallelogram-shaped domains with irregular shapes and sizes. The locations of the domain boundaries can be readily identified based on the prominent contrast features associated with the linear arrays of directionally aligned brighter dots. Moreover, all these domains share a common crystallographic orientation, with their c axes aligned in the same direction. Figures 3(c) and 3(d) show enlarged images of the local areas enclosed by either rectangle C or D, as shown in Fig. 3(a). Areas C and D are in the upper and lower corners, respectively, of the individual domain. A consistent contrast feature recognized in both Figs. 3(c) and 3(d) is the regular arrangement of the pairs of dots with alternating bright and dark intensities (larger and smaller in size, respectively), arranged regularly based on the fcc lattice. Each dot contrast corresponds to an individual atomic column defined in the

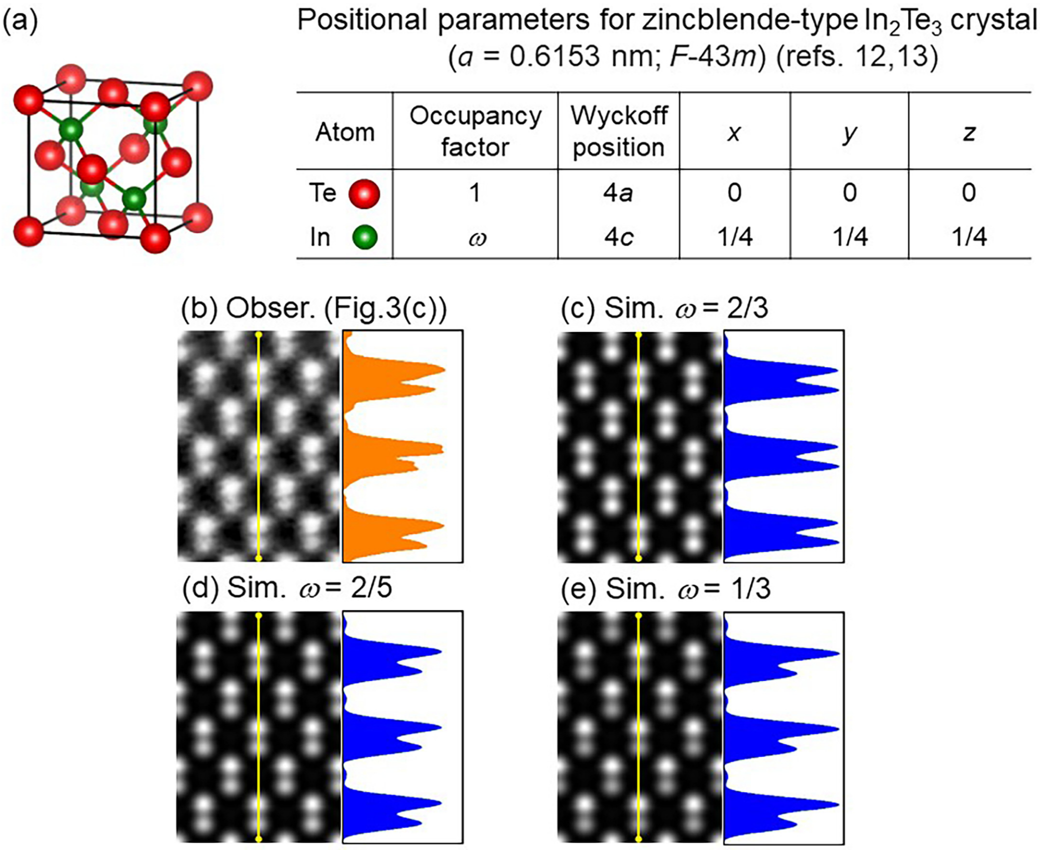

Positional parameters for zincblende-type In_2Te_3 crystal
(a = 0.6153 nm; F-43m) (refs. 12,13)

Atom	Occupancy factor	Wyckoff position	x	y	z
Te ●	1	4a	0	0	0
In ●	ω	4c	1/4	1/4	1/4

FIG. 4. (a) Unit cell of the β-In_2Te_3 phase (zinc-blende type structure) and its positional parameters; a typical probe-corrected atomic-scale HAADF-STEM image recorded in the [110] incidence is shown in (b) and the corresponding simulated images are shown in (c), (d), and (e). The simulated images in (c)–(e) are obtained under the conditions of identical atom positional parameters but different values of the occupancy factor ω assumed for In atoms on the 4c sites shown in (a), which is either 2/3, 2/5, or 1/3. The corresponding image contrast intensity profiles obtained from the straight path running in the longitudinal direction in each image are also shown. These images are illustrated in an 8-bit grayscale mode, where the constituent pixels have 256 different intensity steps ranging from black to white. The parameters used for the image simulations are an accelerating voltage of 200 kV, beam convergence angle of 18 mrad, annular dark-field detector range of 79–120 mrad, and specimen thickness t of ~15 nm.

projection along the [110] viewing direction. To determine the atomic arrangement directly from the image in Fig. 3, the following conditions or situations must be considered. First, the image contrast observable in the HAADF-STEM image is associated with the difference in the atomic numbers of the constituent atoms of the material. Second, the unique crystallographic situation in which no atomic columns containing any mixing sites for In and Te atoms can be defined in the [110] projection, assuming a zinc-blende type structure as the model, must be considered. Third, some of the equivalent sublattice sites for the In atoms are only partially occupied. Considering all these factors involved in the resulting image, the Te columns are expected to exhibit a distinctively higher intensity than the In columns despite the relatively small difference in their atomic numbers (In: 49; Te: 52), as evidenced later. Consequently, a projected atomic structure profile for the β-In_2Te_3 phase is superimposed on the HAADF-STEM image, as shown in Figs. 3(c) and 3(d), where the atomic columns comprising Te and In are indicated in red and green, respectively. These observations confirm that the β-In_2Te_3 phase possesses a matrix finely and intricately subdivided by a specific domain boundary, all of which have their crystallographic c axes pointing completely in the [001] type direction. Furthermore, the results demonstrate that the unit cell of the crystal is regionally inverted between the parallel and antiparallel states within individual domains.

Image simulations were performed to evaluate the obtained atomic-scale HAADF-STEM images and provide sufficient evidence supporting our proposed interpretation of the domain structure in the β-In_2Te_3 crystal. Figure 4(a) shows the unit cell of the β-In_2Te_3 phase together with positional parameters for the crystal, which is a standard representation of a zinc-blende type structure. Figure 4(b) presents the data obtained from the [110] HAADF-STEM image of the local area depicted in Fig. 3(c). In contrast, Figs. 4(c)–4(e) show three different simulated images obtained under identical atomic positional parameters but different values of the occupancy factor ω assigned to In atoms on the 4c sites [Fig. 4(a)], which are either 2/3, 2/5, or 1/3. The images are accompanied by the corresponding image contrast intensity profiles obtained from the straight path running in the longitudinal direction in each image. The simulation case with $\omega = 2/3$, as represented by Fig. 4(c), which is based on a statistically random distribution of the In atoms in the 4c sites, aligns with the fundamental

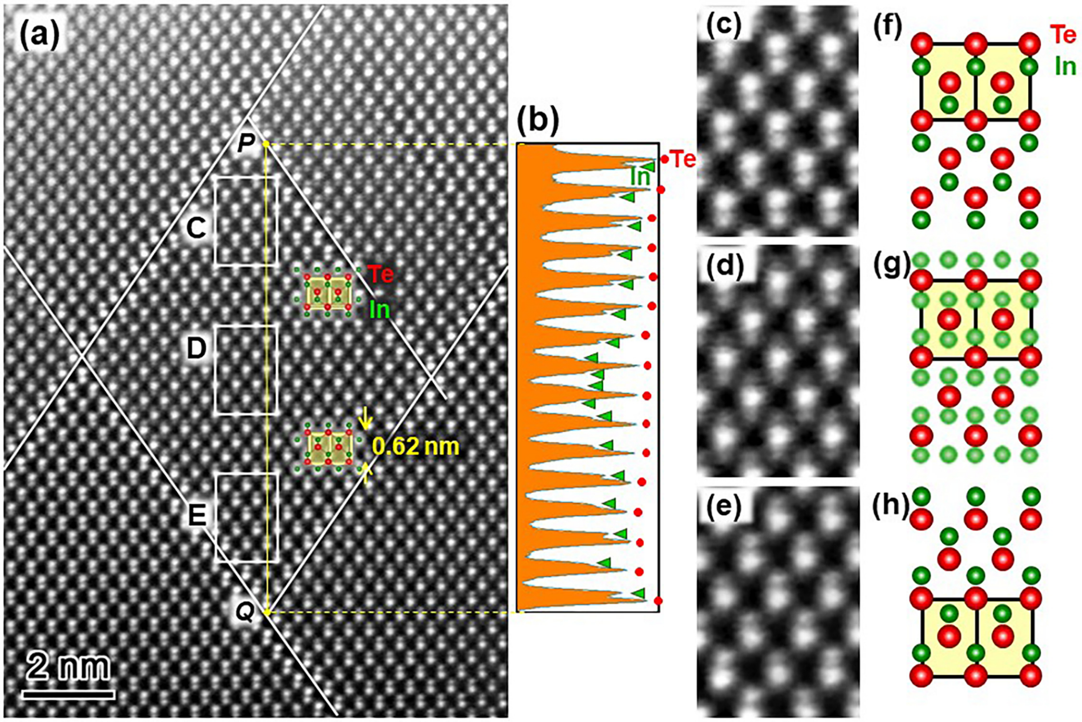

FIG. 5. (a) Enlarged HAADF-STEM [110] image of the local area enclosed by rectangle A in Fig. 3(a). The diamond-shaped region located in the middle shows a complete picture of one individual domain. (b) Image intensity profile obtained from the straight line along the longitudinal direction of the domain, between points *P* and *Q* depicted in (a). (c)–(e) Enlarged images of the area enclosed by rectangles C, D, and E depicted in (a), with (f)–(h) the corresponding frame formats of the projected atomic structure profiles.

principle for stabilizing the covalently bonded In_2Te_3 crystal with 1/3 of the cationic sublattice sites vacant. However, each pair of the dot contrasts in Fig. 4(c) exhibits Te and In dots with approximately comparable intensities and sizes, although each pair of the dot contrasts in Fig. 4(b) comprises brighter (Te) and darker (In) dots with varying intensities. The observed image in Fig. 4(b) is best reproduced by the simulated image resulting from $\omega = 2/5$ [Fig. 4(d)] in all cases. Consequently, data comparison between the observed and simulated images confirmed that appreciable amounts of structural vacancies at the 4*c* sites produced a considerable change in the resulting *Z*-contrast image.

Figure 5(a) shows an enlarged probe-corrected HAADF-STEM image of the local area marked *A* in Fig. 3(a). An individual diamond-shaped domain in the middle, enclosed by four separate {111} type planes represented by solid line segments, was closely examined. Figure 5(b) presents the image contrast intensity profile obtained from the straight path running along the longitudinal direction of the domain between points *P* and *Q*, as illustrated in Fig. 5(a). In Fig. 5(b), the prominent peaks indicated by small circles appear at regular intervals of ~0.62 nm. Each peak is accompanied by shoulder peaks on one or both sides, as marked by arrowheads. The series of shoulder peaks, particularly inspected from either corner to the middle of the domain, indicates a gradual decrease in intensity levels. Based on the preceding discussion, the primary peaks correspond to the atomic columns of Te defined in the [110] projection, whereas the shoulder peaks represent the In columns containing structural vacancies. Notably, the relative positions of the primary and shoulder peaks are gradually inverted between the upper and lower corners. Figures 5(c), 5(d), and 5(e) illustrate the enlarged images of the areas marked as C, D, and E in Fig. 5(a), respectively. These images are accompanied by the corresponding frame formats depicting the projected atomic structure profiles, as illustrated in Figs. 5(f)–5(h). The contrast features appearing in the upper corner of the domain, as shown in Fig. 5(c), exhibit alternating bright and dark dots aligned vertically from top to bottom. This arrangement is reversed for dots in the lower corner, as depicted in Fig. 5(e). In area D, the longer pairs are replaced by three closely spaced dots. Each set of three dots has one brighter dot in the middle with two extra darker dots symmetrically positioned with respect to the brighter dot. The extra dots with reduced intensities can be reasonably identified as individual In columns defined in the [110] projection. This finding suggests the possibility of an unusual situation in which two alternative sublattice sites are available for In atoms simultaneously, particularly in the middle of the domain. The intensity variations observed for individual In columns correspond to the occupancy of In atoms (or structural vacancies) in these sublattice sites. The In columns existing in the middle of the domain have structural vacancies with relatively increased occupancies compared to those present on the upper and lower sides of the domain. Therefore, Figs. 3 and 5 show that the β-In_2Te_3 crystal structure gradually reverses along the *c* axis between the two opposite corners defined along the longitudinal direction of each domain, involving the site conversion of In atoms. The structural vacancies can be assumed to

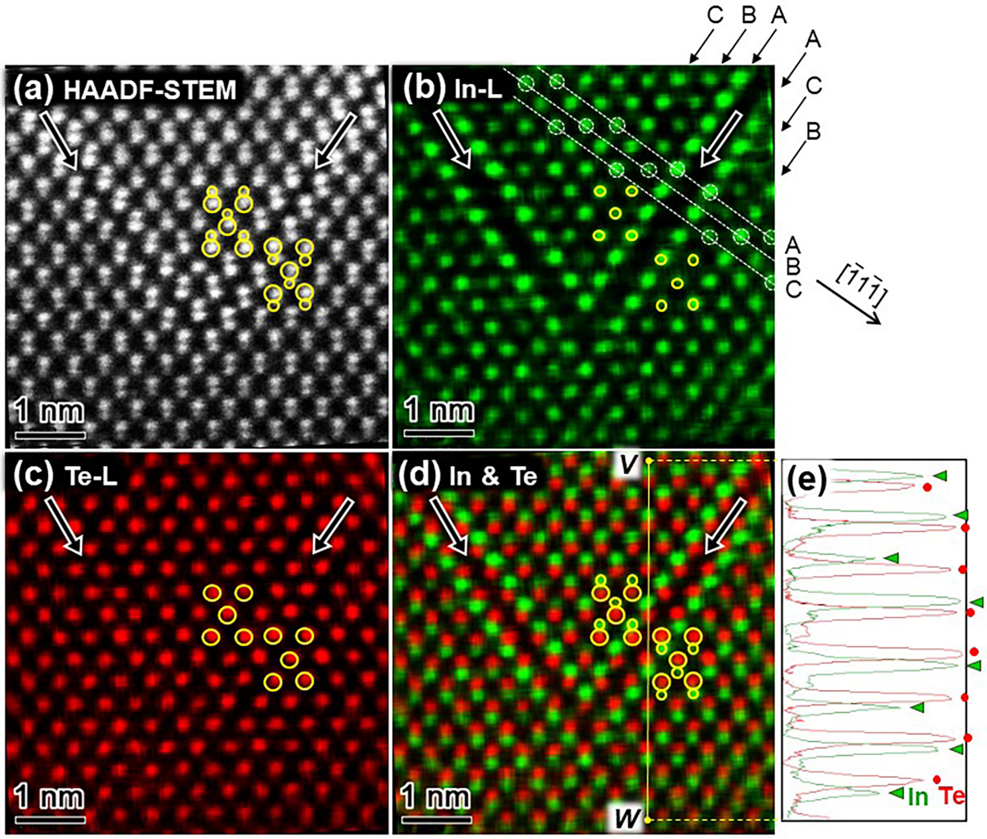

FIG. 6. (a) Enlarged atomic-scale HAADF-STEM image of the local region indicated by Q in Fig. 5(a); (b)–(d) the corresponding atomic-resolution energy-dispersive x-ray spectroscopy (EDXS) mapping images with the respective constituent elements, i.e., In-L, Te-L, and their composite, where the atom columns composed of Te and In are indicated in red and green, respectively; (e) image contrast intensity profile obtained from the straight path running along the longitudinal direction of (d) between points V and W. The EDXS mapping images are displayed in either an 8-bit green-channel or 8-bit red-channel mode. In each image, the two domain boundaries joining together to form a V shape are indicated by arrows. Two sets of half-sectional views of the unit cell are characterized by two different types of circles for visual guidance, where the atom columns corresponding to Te and In are marked by either the larger or the smaller circle.

be distributed randomly among the sublattice sites for the In atoms. However, this systematic approach within each domain exhibits a linear-gradient distribution pattern of the site occupancy, extending from the corner to the middle of the domain.

The combined probe-corrected HAADF-STEM imaging and EDXS mapping analyses provide conclusive evidence for identifying the nature of the domain boundaries present in the β-In_2Te_3 phase. Figure 6(a) illustrates an enlarged atomic-scale HAADF-STEM image from the boundary intersection marked as Q in Fig. 5(a). In contrast, Figs. 6(b)–6(d) present the corresponding atomic-resolution EDXS mapping images, each displaying the respective constituent elements separately: In-L, Te-L, and their composite. Figure 6(e) shows the image contrast intensity profile obtained from the straight path running along the longitudinal direction in the image in Fig. 6(d) between points V and W. In each of the images from Fig. 6(a) to Fig. 6(d), the locations of the two domain boundaries intersecting to form a V shape are indicated by thick arrows. On the adjacent domain edges on the right side, two sets of half-sectional views of the unit cell are characterized by two different types of circles for visual guidance, where the atomic columns corresponding to Te and In are marked by either a larger or a smaller circle. The atomic configuration is vertically flipped across each boundary. This phenomenon is attributed to a change from one of the stacking sequences of the In$\{111\}$ sublayers to the other one, as represented by Cc-Bb-Aa-(gap)-cA-bC-aB, where the assignments of the planes in the $[\bar{1}1\bar{1}]$ direction are expressed by capital letters A, B, and C for the In sublayers and the corresponding small letters for the Te sublayers. These domain boundaries, referred to as 180° domains, are analogous to one of the structural characteristics observed in ferroelectric [33–37,40] and ferromagnetic materials. Our observations confirm that the results presented in Figs. 3–6 do not represent specific local phenomena but are valid across the entire material.

The intensity distribution of the dot contrast attributed to the Te columns remains relatively homogeneous across the entire micrograph [Fig. 6(c)]. In contrast, the intensity of the In columns varies considerably depending on location [Fig. 6(b)]. In Fig. 6(b), two sets of three consecutive In$\{111\}$ sublayers are indicated by the pairs A-(gap)-A, B-(gap)-C, and C-(gap)-B (A-A, B-C, and C-B, respectively, for short), with a domain interface between the two sets. Each pair of sublayers exhibits similar contrast features. The first pair (A-A), located on either side of the boundary interface,

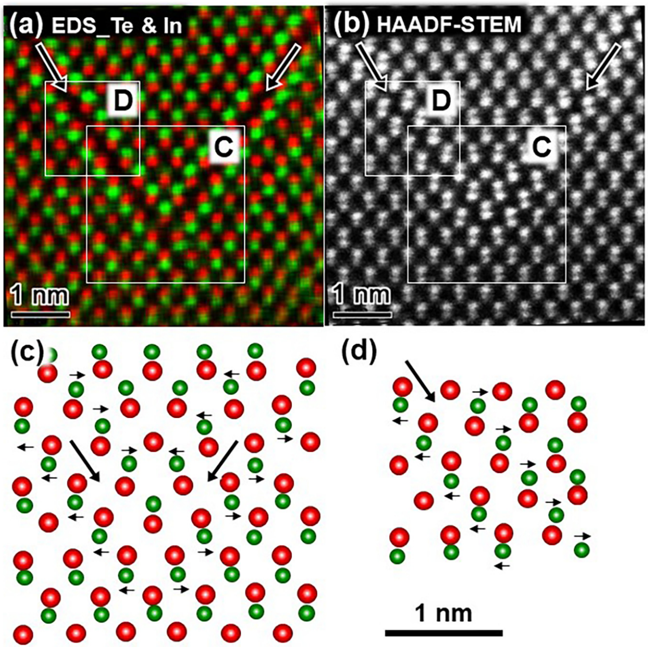

FIG. 7. (a),(b) Selected pair of EDXS mapping and HAADF-STEM images shown in Fig. 6. (c),(d) Twofold enlarged atomic arrangement in the areas marked C or D in (a) or (b). In atoms in adjacent areas of the boundary interfaces are displaced laterally to distance themselves away from the boundary.

exhibits maximal intensity for the constituent dot contrasts, except for minor details. One can infer from Fig. 4 that In atoms occupy more than two-thirds of the sublattice sites belonging to the corresponding atomic columns. In contrast, the next pair (B-C), located second nearest to the boundary interface, exhibits a significant reduction in the intensity of the constituent dot contrasts, indicating that the corresponding atom columns accommodate the highest vacancy occupancy. The third pair (C-B), exhibits constituent dot contrasts slightly brighter than those of sublayer B-C, signifying a lower vacancy occupancy than that of sublayer B-C. The subsequent sublayers after C-B exhibit structural vacancies that increase gradually, as shown in Fig. 5. The intensity variation of the dot-contrast signals due to the In columns described above are well illustrated in Fig. 6(e). Figure 6(e) also shows that each of the pairs of dot contrasts due to the Te columns, belonging to the third-nearest pair from the gap, experiences a considerable decrease in the intensity level compared to those of the other pairs. This observation confirms that the intensity distribution of the dot contrast attributed to the Te columns is not completely homogeneous, indicating that vacancies may exist at the sublattice sites for the Te atoms in the domain interior.

Another notable feature is the consistent atomic displacement observed in the In atoms adjacent to the domain interfaces. Figures 7(a) and 7(b) show the same set as that depicted in Figs. 6(d) and 6(a) but in a differently highlighted version. Figures 7(c) and 7(d) illustrate the twofold enlarged atomic arrangements in the areas marked C and D in Fig. 7(a). The In atoms located on both sides of the boundaries undergo lateral displacement from the average positions in two opposite directions away from the boundary interfaces. Consequently, the local $\mathrm{In}(\bar{1}11)$ and $\mathrm{In}(1\bar{1}1)$ sublattice spacings increase considerably. This displacement behavior can be attributed to the unique electrostatic potential generated near the 180° boundaries.

IV. DISCUSSION

This study revealed previously unknown features of the domain structure formed in β-$\mathrm{In_2Te_3}$ crystals. The probe-corrected STEM observations combined with atomic-scale EDXS analysis enabled us to resolve a debate on the issue. Eventually, the domain boundaries were identified as 180° domain walls, where the atomic structure of the crystal was inverted between parallel and antiparallel states. Contrary to earlier assumptions of structural vacancies in the crystal segregating into $\{111\}$-subset planes, our findings revealed a random distribution of structural vacancies throughout the matrix. However, these vacancies systematically occupied sublattice sites mostly for In atoms. Consequently, the newly discovered 180° domain structure exhibited several distinctive characteristics. Although the ferroelectric crystals had uniform crystalline interiors bounded by 180° domain walls with a single crystal variant, the domain interior of the β-$\mathrm{In_2Te_3}$ crystal exhibited a series of regionally varied structures attributed to the systematic distribution pattern of structural vacancies. Consequently, regional and gradual reversal of the local structural configuration occurred along the c axis between the two opposite corners defined along the longitudinal direction of each parallelogram-shaped domain.

Structural reversal involves site conversion for In atoms, as explained below. We considered two different sublattice sites available for In atoms: In1(1/4, 1/4, 1/4) in the standard xyz-coordinate system defined for the unit cell of the present crystal, and In2(1/4, 1/4, $-1/4$). The contrasting variations observed in Figs. 5(c)–5(e) suggest a gradual conversion from In1 to In2 lattice sites. Notably, when we examined a single atom column, the In atoms and structural vacancies were randomly distributed in the In1 or In2 sites. The appearance of the three-dot contrast in Fig. 5(d) represents an intermediate stage during site conversion between In1 and In2. The intensity level of the dot-contrast signals is correlated with the site occupancy of In atoms or the mixing ratio of In atoms (or the structural vacancies) at the sublattice sites. This mixing state can be expressed as $(1-x)\mathrm{In1}+xV$, where V stands for vacancy and x stands for the mixing ratio of the structural vacancies. Mathematically, x increases gradually from 0 to 1 as the area for inspection shifts from C to D, as shown in Fig. 5(a). However, in reality, certain lower and upper limits of x exist that vary within the range of 0–1. The upper limit of x is below 1, where the occupancy rate of the vacancies in one individual In1 column reaches the highest possible level around the middle area D. When shifted downward from the critical spot represented by the upper limit x in the domain, some of the In atoms begin to occupy the In2 sites instead of the In1 sites. This transition is described by the expression $(1-y)\mathrm{In2}+yV$, where the mixing ratio y decreases gradually from the upper limit below 1 to the lower limit above 0. Alternatively, the structural vacancies are spatially distributed

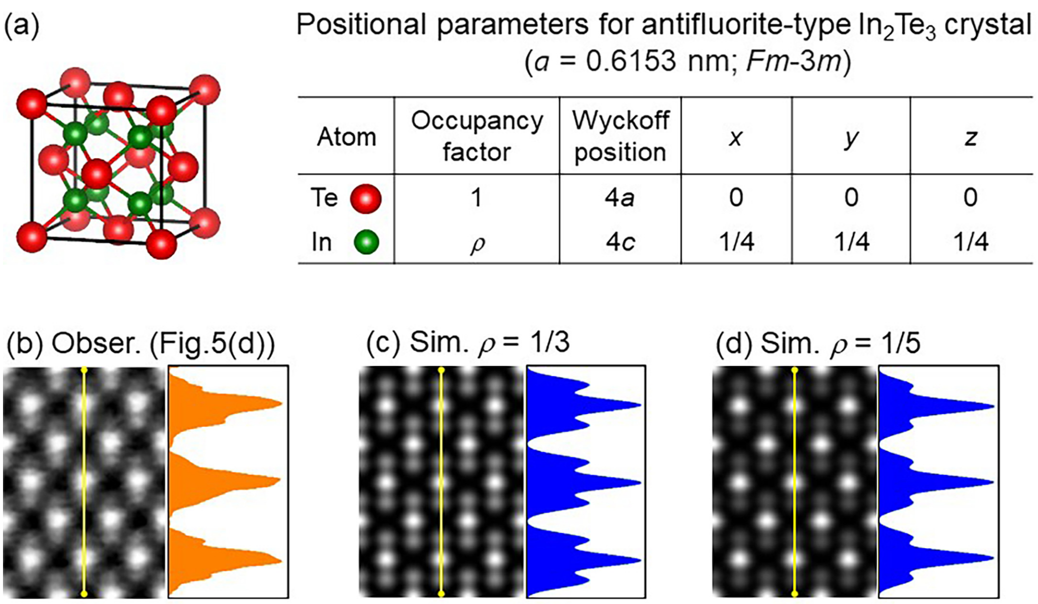

Positional parameters for antifluorite-type In_2Te_3 crystal
(a = 0.6153 nm; Fm-3m)

Atom	Occupancy factor	Wyckoff position	x	y	z
Te ●	1	4a	0	0	0
In ●	ρ	4c	1/4	1/4	1/4

FIG. 8. (a) Unit cell of a virtual model of antifluorite type In_2Te_3 crystal structure and its positional parameters; a typical probe-corrected atomic-scale HAADF-STEM image recorded in the [110] incidence is shown in (b) and the corresponding simulated images are shown in (c) and (d). The simulated images in (c) and (d) are obtained under the conditions of identical atom positional parameters but different values of the occupancy factor ρ assumed for In atoms on the 4c sites shown in (a), which is either 1/3 or 1/5, respectively. The corresponding image contrast intensity profiles obtained from the straight path running in the longitudinal direction in each image are also shown. These images are displayed in an 8-bit grayscale mode, where the constituent pixels have 256 different intensity steps ranging from black to white. The parameters used for the image simulations are an accelerating voltage of 200 kV, beam convergence angle of 18 mrad, annular dark-field detector range of 79–120 mrad, and specimen thickness t of ∼15 nm.

in a linear-gradient pattern considering the site occupancy, extending from either corner to the middle of each individual domain.

The aforementioned structural characteristics may be more easily understood in terms of a continuous regional phase change occurring within the domain. Here, we assume that the middle of the domain comprises an antifluorite type structure with atomic positions of Te at (0, 0, 0) and In/V at (±1/4, ±1/4, ±1/4) denoting the In1 and In2 sites, instead of the zinc-blende type with Te at (0, 0, 0) and In/V at (1/4, 1/4, 1/4). For $x = 0$ and $y = 1$ or vice versa, the former structure type corresponds exactly to the latter. To provide a more quantitative analysis of the occupancy factor for the In atoms, we performed image simulations to evaluate the obtained atomic-scale HAADF-STEM image from the middle of the domain. Figure 8(a) shows the unit cell of a virtual model of the antifluorite type In_2Te_3 crystal together with its positional parameters. Figure 8(b) illustrates the data obtained from the [110] HAADF-STEM image of the local area depicted in Fig. 5(d). In contrast, Figs. 8(c) and 8(d) present two different simulated images obtained under identical atomic positional parameters but different values of the occupancy factor ρ assigned to In atoms on the 4c sites [Fig. 8(a)], which are either 1/3 or 1/5. The images are accompanied by the corresponding image contrast intensity profiles obtained from the straight path running in the longitudinal direction in each image. Both simulated images well reproduced the regular arrangement of the three dots, and the simulation case with $\rho = 1/5$ [Fig. 8(d)] was particularly observed to provide a better match for the observed image than $\rho = 1/3$ [Fig. 8(c)]. Thus, data comparison between the observed and simulated images corroborated this interpretation. The present results confirm that the middle region of the domain comprises the antifluorite type In_2Te_3 crystal structure with a relatively low occupancy factor ($\rho = 1/5$) at the 4c sites compared to that ($\omega = 2/5$) observed for a zinc-blende type crystal structure present on the upper and lower sides of the domain.

Ferroelectric materials are known to adopt a stable, minimum-energy arrangement of domains and domain walls aligning with their boundary conditions, such as the overall average strain, polarization states caused by imposed displacements, and electric charges at the crystal surfaces [37]. The formation of 180° domain walls in ferroelectric crystals, which separate the regions of the crystal lattice with antiparallel polarizations, minimizes the electrostatic energy. A similar energy minimization effect may dominate the In_2Te_3 crystal when annealed at 650°C, imposing the subsection of the matrix by introducing the 180° domain boundaries. Ferroelectrics exhibit spontaneous electric polarization owing to the dipoles formed by the displacement of charged ions inside the crystal unit cell. Antiferroelectrics also enable the formation of local electric dipoles. However, unlike ferroelectrics, the total macroscopic spontaneous polarization is zero because adjacent dipoles cancel each other. In this context, the present β-In_2Te_3 crystals can be categorized as antiferroelectrics. Specifically, the corner portions of each domain that are located further away from the boundary than the interlattice spacing between the third-nearest In{111} sublayers and the geometrical center plane in the gap as represented by either C-(gap) or (gap)-B in Fig. 6(b), which is dominated by the zinc-blende type structure, have roughly the same number of structural vacancies as the middle portion dominated by the antifluorite type structure. The occupancy factors for the In atoms on the 4c sites were estimated to be $\omega = 2/5$ for the corner identified as the zinc-blende type structure [Fig. 4(d)] and $\rho = 1/5$ for the middle identified as the antifluorite type structure [Fig. 8(d)]. This finding indicates that $x_1V + x_2V$ remains at a constant value of 3/5 over the domain interior from the corner to the middle, where x_1 and x_2 denote the mixing ratios of the vacancies on the In1 and In2 columns, respectively. Although regional variation exists in the distribution of the structural vacancies along the longitudinal direction of the domain, the mixing ratios of the vacancies remain at approximately the same level over most of the domain interior. Therefore, it can be reasonably deduced that the electric charges are mostly constant over the domain interior or decreased slowly towards the domain center. In this case, local electric dipoles are less pronounced in the domain interior. However, this situation does not apply to the domain-edge regions, as detailed below.

The β-In$_2$Te$_3$ crystal appears to have permanent dipole moments generated locally in the edge regions of the 180° domain boundaries. As indicated above, the mixing ratio for the In atoms for most of the domain interior was estimated to be 2/5 on average, and this value is measurably less than the reference value of 2/3, which was determined according to a general principle for stabilizing a covalently bonded In$_2$Te$_3$ crystal. The remaining In atoms with a ratio of 4/15 ($\sim$27%) are concentrated at several particular locations, such as in the pairs of In$\{111\}$ sublayers, which are located on either side of the boundary interface (see Fig. 6). The first-nearest In$\{111\}$ sublayers represented by A-A may represent a positively charged region because it contains the highest possible concentration of In (i.e., a cationic element), whereas the next and following sublayers constitute a negatively charged region because of the relatively lower concentrations of In compared to the first region. Therefore, the local dipole generated in the domain edge points outward along the longitudinal direction of the domain, parallel to the [001] type direction, by canceling out the transverse component of the dipole moment because of the crystal symmetry. Alternatively, each domain in the crystal may comprise two antiferroelectric subdomains represented by two opposite electric dipoles that are lined up at the upper and lower corners in a tail-to-tail arrangement [40]. In the middle of the two subdomains, a relatively wide domain wall consisting of the nonpolar antifluorite type structure lies in parallel to the $\{001\}$ type lattice plane. This characteristic is not so unusual, because similar observations in which a strip of a nonpolar crystal region exists as a buffer zone in between two separate antiferroelectric domains were also found in some other ferroelectric materials [33,36]. As illustrated in Fig. 5(a), near the 180° domain boundaries, two opposite dipoles arising from the adjacent domains should face each other closely with a head-to-head arrangement across the interface. This configuration may generate an intense compressional stress field for the cationic atoms such as In within its sphere of influence. This compressional stress could be a crucial factor contributing to the anomalous displacements imposed on the In atoms present at the boundary edges, as shown in Fig. 7. The minimization of the system energy with respect to the depolarization field and mechanical strain is responsible for the coexistence of the two types of domains, as observed in the β-In$_2$Te$_3$ crystal.

The two unique features of the local structural environment adjacent to the 180° domain boundaries are notable: first, each pair of In$\{111\}$ sublayers located on either side of the boundaries has In atoms accommodated maximally at the 4c sites belonging to the constituent [110]-In columns; second, the lattice spacing of the In$\{111\}$ sublayers increases locally in the adjacent areas of the 180°-domain boundaries. These structural inhomogeneities account for the contrast anomalies identified in the HRTEM images, as highlighted by the paired arrows in Fig. 2(c). The diffuse maxima between the fundamental spots observed in the SAD pattern of Fig. 2(b) are attributed to the irregular distribution of the double-spaced $\{111\}$ planes, which were decorated by the excessive concentration of In atoms. Based on the HRTEM and SAD data alone, we could not specify the cause of the conspicuous contrast feature associated with the double-spaced $\{111\}$ planes, as illustrated in Fig. 2(c). The present HAADF-STEM observations contributed to the identification of the origin.

V. CONCLUSIONS

The structural characteristics of nanosized domains formed in β-In$_2$Te$_3$ crystals were thoroughly investigated using probe-corrected STEM imaging and EDXS analysis. Consequently, we reevaluated previous interpretations of this issue and established a real crystal structure for these domains. The major conclusions can be summarized as follows:

(1) The β-In$_2$Te$_3$ crystal exhibits a uniform crystalline matrix based on a zinc-blende type structure (cell parameter: $a = 0.6153$ nm; space group $F\bar{4}3m$). However, at the microscopic scale, the crystal is finely subdivided into 180° domains, where the local crystal structure undergoes inversion between parallel and antiparallel states.

(2) Every individual domain maintains the crystallographic c axis, all pointing in the same direction, parallel to the [001] type direction. However, within each domain, the local structural configuration regionally and gradually reverses along the c axis between the two opposite corners defined along the longitudinal direction of the domain. A structural reversal occurs, involving both the random but linear-gradient spatial distribution pattern of structural vacancies induced in the [001] type direction and the continuous regional phase change from the zinc-blende type structure having a space group of $F\bar{4}3m$ with Te at (0, 0, 0) and In/V at (1/4, 1/4, 1/4) to the antifluorite type structure having a space group of $Fm\bar{3}m$ with Te at (0, 0, 0) and In/V at (±1/4, ±1/4, ±1/4).

(3) The β-In$_2$Te$_3$ crystal facilitates the formation of local electric dipoles within each domain because of the systematic spatial distribution pattern of the structural vacancies, exhibiting zero macroscopic polarization. Each domain in the crystal comprises two antiferroelectric subdomains represented by two opposite local dipoles aligned in a tail-to-tail arrangement. In the middle of the two subdomains, a relatively wide domain wall consisting of a nonpolar antifluorite type structure lies parallel to the $\{001\}$ type lattice plane. The coexistence of these two different types of domains, as observed in the β-In$_2$Te$_3$ crystal, results from the minimization of system energy considering the depolarization field and mechanical strain. The other types of $A_2^{\mathrm{III}}B_3^{\mathrm{VI}}$ compounds are also likely to have structural characteristics similar to those of nanosized

domains, which could have significant effects on their physical properties.

ACKNOWLEDGMENTS

Part of this work was supported by the Tohoku University Microstructural Characterization Platform in the Nanotechnology Platform Project sponsored by the Ministry of Education, Culture, Sports, Science, and Technology (MEXT), Japan.

The authors declare that they have no competing financial interests or personal relationships that may have influenced the work reported in this study.

[1] W. Li, X.-F. Cai, N. Valdes, T. Wang, W. Shafarman, S.-H. Wei, and A. Janotti, In_2Se_3, In_2Te_3, and $In_2(Se, Te)_3$ alloys as photovoltaic materials, J. Phys. Chem. Lett. **13**, 12026 (2022).

[2] J. Zhen, W. Deng, C. Li, J. Feng, S. Zhang, S. Wan, G. Wang, H. Dong, R. A. Susilo, and B. Chen, Superconductivity in In_2Te_3 under compression induced by electronic and structural phase transitions, J. Phys. Chem. Lett. **13**, 1226 (2022).

[3] X. Yang, A. Banerjee, Z. Xu, Z. Wang, and R. Ahuja, Interfacial aspect of $ZnTe/In_2Te_3$ heterostructures as an efficient catalyst for the hydrogen evolution reaction, J. Mater. Chem. A **7**, 27441 (2019).

[4] P. Zhao, Y. Ma, X. Lv, M. Li, B. Huang, and Y. Dai, Two-dimensional III_2-VI_3 materials: Promising photocatalysts for overall water splitting under infrared light spectrum, Nano Energy **51**, 533 (2018).

[5] V. Sowjanya, K. V. Bangera, and G. K. Shivakumar, Structural, electrical and optical properties of stoichiometric In_2Te_3 thin films, Ceram. Int. **43**, 3748 (2017).

[6] J. Yao, Z. Deng, Z. Zheng, and G. Yang, Stable, fast UV-Vis-NIR photodetector with excellent responsivity, detectivity, and sensitivity based on α-In_2Te_3 films with a direct bandgap, ACS Appl. Mater. Interfaces **8**, 20872 (2016).

[7] M. Safdar, Z. Wang, M. Mirza, F. K. Butt, Y. Wang, L. Sun, and J. He, Telluride-based nanorods and nanosheets: Synthesis, evolution and properties, J. Mater. Chem. A **1**, 1427 (2013).

[8] M. Safdar, Z. Wang, M. Mirza, C. Jiang, and J. He, Crystalline indium sesquitelluride nanostructures: Synthesis, growth mechanism and properties, J. Mater. Chem. **22**, 19228 (2012).

[9] J. Ye, Y. Nakamura, and O. Nittono, Vacancy ordered structure of the III_2VI_3 compound semiconductor $(Ga_xIn_{1-x})_2Se_3$ studied by electron diffraction and microscopy, Philos. Mag. A **73**, 169 (1996).

[10] P. C. Newman, Crystal structures of adamantine compounds, J. Phys. Chem. Solids. **24**, 45 (1963).

[11] D. Lubbers and V. Leute, The crystal structure of β-Ga_2Se_3, J. Solid State Chem. **43**, 339 (1982).

[12] H. Hahn and W. Klinger, Über die kristallstrukturen des In_2S_3 und In_2Te_3, Z. Anorg. Chem. **260**, 97 (1949) (in German).

[13] H. Hahn, Zur struktur der galliumchalkogenide, Angew. Chem. **64**, 203 (1952) (in German).

[14] H. Inuzuka and S. Sugaike, On In_2Te_3, its preparation and lattice constant, Proc. Jpn. Acad. **30**, 383 (1954).

[15] J. C. Woolley and B. R. Pamplin, The ordered crystal structure of In_2Te_3, J. Less-Common Met. **1**, 362 (1959).

[16] A. I. Zaslavskii and V. M. Sergeeva, The polymorphism of In_2Te_3, Sov. Phys. Solid State **2**, 2556 (1961).

[17] A. I. Zaslavskii, N. F. Kartenko, and Z. A. Karachentseva, Unit cell and space group of α-In_2Te_3, Sov. Phys. Solid State **13**, 2152 (1972).

[18] P. J. Holmes, I. C. Jennings, and J. E. Parrott, Precipitation phenomena in In_2Te_3, J. Phys. Chem. Solids **23**, 1 (1962).

[19] P. C. Newman, Ordering in $A_2^{III}B_3^{VI}$ compounds, J. Phys. Chem. Solids **23**, 19 (1962).

[20] T. Karakostas and N. A. Economou, Ordered phases of In_2Te_3, Phys. Status Solidi A **31**, 89 (1975).

[21] R. R. Desai, D. Lakshminarayana, P. B. Patel, P. K. Patel, and C. J. Panchal, Growth and structural properties of indium sesquitelluride (In_2Te_3) thin films, Mater. Chem. Phys. **94**, 308 (2005).

[22] W. Klemm and H. U. Von Vogel, Messungen an gallium- und indium-verbindungen. X. Über die chalkogenide von gallium und indium, Z. Anorg. Chem. **219**, 45 (1934) (in German).

[23] P. A. Shunk, *in Constitution of Binary Alloys: Second Suppl*, McGraw-Hill Series in Materials Science and Engineering (McGraw-Hill, New York, NY, 1969).

[24] V. P. Zlomanov, M. S. Sheiman, V. N. Demin, and B. Legendre, Phase diagram and thermodynamic properties of phases in the In-Te system, J. Phase Equilib. **22**, 339 (2001).

[25] C. E. T. White and H. Okamoto, *in Phase Diagram of Indium Alloys and their Engineering Applications* (ASM International, Utica, NY, 1992), p. 265.

[26] S. Abe, Y. Nakamura, and O. Nittono, Order-mesoscopic transformation in compound semiconductor In_2Te_3, Proc. Pac. Rim Int. Conf. Adv. Mater. Process. **1**, 1393 (1998).

[27] S. Abe, Y. Nakamura, and O. Nittono, Mesoscopic phase transformation in In_2Te_3 compound semiconductor, in *Proceedings of Solid-Solid Phase Transformation* (The Japan Institute of Metals, Sendai, Japan), p. 1417.

[28] K. Kurosaki, H. Matsumoto, A. Charoenphakdee, S. Yamanaka, M. Ishimaru, and Y. Hirotsu, Unexpectedly low thermal conductivity in natural nanostructured bulk Ga_2Te_3, Appl. Phys. Lett. **93**, 012101 (2008).

[29] S. Yamanaka, M. Ishimaru, A. Charoenphakdee, H. Matsumoto, and K. Kurosaki, Characterization of $(Ga, In)_2Te_3$ with self-assembled two-dimensional vacancy planes, J. Electron. Mater. **38**, 1392 (2009).

[30] M. Guymont, A. Tomas, and M. Guittard, The structure of Ga_2Te_3 an x-ray and high-resolution electron microscopy study, Philos. Mag. A **66**, 133 (1992).

[31] E. Kim, K. Kurosawa, M. Ishimaru, H. Muta, and S. Yamanaka, Effect of vacancy distribution on the thermal conductivity of Ga_2Te_3 and Ga_2Se_3, J. Electron. Mater. **40**, 999 (2011).

[32] T. Hanada, Y. Nakamura, Y. Watanabe, and O. Nittono, Two distinct phases in Ga_2Se_3 compound semiconductor, Trans. Mater. Res. Soc. Jpn. **20**, 743 (1996).

[33] C. L. Jia, S. B. Mi, K. Urban, I. Vrejoiu, M. Alexe, and D. Hesse, Atomic-scale study of electric dipoles near charged and uncharged domain walls in ferroelectric films, Nat. Mater. **7**, 57 (2008).

[34] C. T. Nelson, B. Winchester, Y. Zhang, S. J. Kim, A. Melville, C. Adamo, C. M. Folken, S. H. Baek, C. B. Eom, D. G. Shlom, L. Q. Chen, and X. Pan, Spontaneous vortex nanodomain arrays at ferroelectric heterointerfaces, Nano Lett. **11**, 828 (2011).

[35] C. L. Jia, K. W. Urban, M. Alexe, D. Hesse, and I. Vrejoiu, Direct observation of continuous electric dipole rotation in flux-closure domains in ferroelectric Pb(Zr,Ti)O_3, Science **331**, 1420 (2011).

[36] C. L. Jia, L. Jin, D. Wang, S-B. Mi, M. Alexe, D. Hesse, H. Reichlova, X. Marti, L. Bellaiche, and K. W. Urban, Nanodomains and nanometer-scale disorder in multiferroic bismuth ferrite single crystals, Acta Mater. **82**, 356 (2015).

[37] H. Wu, L. Li, L. Z. Liang, S. Liang, Y. Y. Zhu, and X. H. Zhu, Recent progress on the structural characterizations of domain structures in ferroic and multiferroic perovskite oxides: A review, J. Eur. Ceram. Soc. **35**, 411 (2015).

[38] K. Ishizuka, A practical approach for STEM image simulation based on the FFT multislice method, Ultramicroscopy **90**, 71 (2002).

[39] K. Momma, VESTA (Visualization for Electronic and Structural Analysis), https://jp-minerals.org/vesta/en/.

[40] Y. H. Hu, H. M. Chan, Z. X. Wen, and M. P. Harmer, Scanning electron microscopy and transmission electron microscopy study of ferroelectric domains in doped $BaTiO_3$, J. Am. Ceram. Soc. **69**, 594 (1986).